Applied Catalysis B: Environmental 243 (2019) 771–779

Contents lists available at ScienceDirect

Applied Catalysis B: Environmental

journal homepage: www.elsevier.com/locate/apcatb

Enhanced photocatalytic CO_2 reduction to methane over $WO_3 \cdot 0.33H_2O$ via Mo doping

Haipeng Wang[a,b], Ling Zhang[a], Kefu Wang[a,b], Xiang Sun[a,b], Wenzhong Wang[a,*]

[a] State Key Laboratory of High Performance Ceramics and Superfine Microstructure, Shanghai Institute of Ceramics, Chinese Academy of Sciences, 1295 Dingxi Road, Shanghai 200050, People's Republic of China

[b] University of Chinese Academy of Sciences, Beijing 100049, People's Republic of China

ARTICLE INFO

Keywords:
CO_2 photoreduction
Mo doping
CO_2 activation
Water oxidation
Proton insertion

ABSTRACT

Photocatalytic CO_2 reduction is a promising strategy to address environmental and energy issues that are vexing the modern society. However, the efficiency of CO_2 photoreduction into fuels such as methane (CH_4) is substantially restricted by high CO_2 activation barrier and inefficient proton supply. Here, Mo-doped $WO_3 \cdot 0.33H_2O$ nanorods have been synthesized and Mo doping in $WO_3 \cdot 0.33H_2O$ dramatically increased the CH_4 production yield by 5.2 times from 1.02 to 5.3 μmol g_{cat}^{-1} h^{-1} under water vapor without the assistant of any sacrificial agent or noble metal. The Mo doping proves capable of facilitating CO_2 activation by improving the ability to store and localize photogenerated electrons and boosting the transfer of photoexcited electrons to adsorbed CO_2. In addition, proton and electron insertion converts $WO_3 \cdot 0.33H_2O$ into tungsten bronze ($H_xWO_3 \cdot 0.33H_2O$) under light irradiation, guaranteeing required electrons and protons for CO_2 reduction. The enhanced water oxidation of Mo-doped $WO_3 \cdot 0.33H_2O$ promotes proton supply and insertion process, improving the hydrogenation process of the carbon intermediate to generate CH_4. The combined action of the enhanced CO_2 activation and water oxidation with efficient proton and electron insertion improves the performance of CO_2 photoreduction to CH_4. This work might help to shed light on deeper insights into the design of CO_2 photoreduction catalysts.

1. Introduction

The inexorable rise of carbon dioxide level in the atmosphere which has already exceeded 400 ppm in 2015, has attracted worldwide attention on controlling CO_2 emissions [1,2]. Photocatalytic CO_2 reduction has been regarded as one of the most promising strategies to address the environmental and energy issues [3–6]. However, CO_2 is of high thermodynamical stability due to a high bond energy of C=O (~750 kJ mol^{-1}), which limits the conversion efficiency. The adsorption of CO_2 on a catalyst surface offers one way of activating the inert molecule for reduction [7,8]. It is considered that CO_2 adsorption causes the formation of a partially charged species $CO_2^{\delta-}$ through interactions with surface atoms, resulting in the weakening of C=O bond [8,9]. Promoting the transfer of electrons from the catalyst to CO_2 is the key to activate CO_2. It has been reported that the surface negative charge density generally determines the adsorption and activation of CO_2 [10–12]. Currently, noble metals loading is a common approach to improve the surface negative charge density to enhance the CO_2 activation and reduction, but the high cost and limited abundance of noble metals hinder their wide application [13–17]. For non-noble metal systems, the introduction of low valence metal species with trapped excess electrons has also been proved to be a powerful method to promote CO_2 adsorption and activation, which may be a more economical and accessible solution [18–22].

According to recent reports, the WO_3 with low valence metal species is found to be a promising material for CO_2 reduction. The enhanced CO_2 activation was achieved by hydrogen-treated WO_3 owing to the introduction of oxygen vacancies and W^{5+} into the materials, even though its conduction band edge is rather positive [23–25]. However, the harsh requirements for experimental conditions, such as high-temperature hydrogen reduction of WO_3, become the new problems [23–25]. Moreover, for CO_2 reduction reaction with the hydrogen-treated WO_3, most of the product is CO instead of CH_4 [23,24]. Therefore, designing a simple WO_3 with low valence metal species and improved photocatalytic activity to reduce CO_2 to CH_4 is necessary. Foreign ion doping is a simple and effective method to regulate the electronic structure of photocatalysts and thus may change the valence state of elements, offering the opportunity to introduce low valence metal species of WO_3 [26,27]. As Mo possesses a similar ionic size, but different d-electron structure and electronegativity from W, the Mo

* Corresponding author.
E-mail address: wzwang@mail.sic.ac.cn (W. Wang).

https://doi.org/10.1016/j.apcatb.2018.11.021
Received 29 August 2018; Received in revised form 30 October 2018; Accepted 8 November 2018
Available online 08 November 2018
0926-3373/ © 2018 Elsevier B.V. All rights reserved.

doping may allow tuning the electronic structure of WO_3 and introducing active sites [28,29]. It has been found that Mo doping could increase the ratio of low valence metal species (W^{5+}, Mo^{5+}) in WO_x, which could trap electrons and promote photo-induced electron-hole separation, leading to enhanced redox ability [28–31]. In addition, the Mo doping in tungsten oxide could highly facilitate the photogenerated electrons transfer from active sites to adsorbate, which makes reduction reactions more efficient [32]. Taking these into account, Mo doping in WO_3 may be an effective way to regulate the low valence metal species and improve electron donating power to improve CO_2 reduction efficiency.

Furthermore, due to the ability of WO_3 to form hydrogen bronzes with Brønsted protons and excess electrons in its lattice, photoactive $WO_3{\cdot}nH_2O$ could supply the required electrons and protons for subsequent protonation [24,33,34]. Wang *et at.* [35] have confirmed that the $WO_3{\cdot}H_2O$ with outstanding electron and proton conductivity played an indispensable role in the conduction of the proton for the hydrogenation process, and similarly, this process would be also suitable for conducting proton to reduce CO_2 to CH_4.

In this work, Mo-doped hexagonal $WO_3{\cdot}0.33H_2O$ (noted as Mo-WO) nanorods with diameter of 5–10 nm have been synthesized by a Na_2SO_4 assisted hydrothermal method. Mo doping in WO dramatically increased the CH_4 production yield by 5.2 times from 1.02 to 5.3 μmol $g_{cat}{}^{-1}\,h^{-1}$ under atmospheric CO_2 concentration (about 400 ppm) with the CH_4 selectivity improved from 27.3% to 61.2%, while corresponding experiments and characterizations indicated that the boosted performance was expected to derive from enhanced CO_2 activation and water oxidation with efficient proton and electron insertion.

2. Experimental section

2.1. Catalyst preparation

All chemicals involved were of analytical grade and used without further purification. WO nanorods were synthesized by hydrothermal method [36,37]. Typically, 10 mL of hydrochloric acid (3 M) was added to 20 mL of sodium tungstate ($Na_2WO_4{\cdot}2H_2O$) solution (0.075 M) under stirring. When a light-yellow precipitate of amorphous tungstic acid appeared, the mixture was separated by filtration, after which deionized water (30 mL) and a certain amount of sodium sulfate (1.8 g) were immediately added to the solid precipitate. After ultrasonic concussion for 10 min, the system was transferred into a Teflon-lined stainless steel autoclave and heated at 180 °C for 12 h. The products were filtered and washed thoroughly with deionized water and freeze drying overnight.

As for Mo-doped WO nanorods, $Na_2WO_4{\cdot}2H_2O$ and $Na_2MoO_4{\cdot}2H_2O$ of different stoichiometric ratios (Mo:W = 1%, 3%, 5%) were first dissolved in deionized water (20 mL, W + Mo = 1.5 mmol), while the subsequent process was the same as that of WO nanorods. The corresponding products were denoted as 1%Mo-WO, 3%Mo-WO, 5%Mo-WO, respectively.

2.2. Characterization

The XRD characterization of the samples was carried out by a Rigaku Miniflex II desktop X-ray diffractometer with an operating voltage of 30 kV and current of 100 mA, while the wavelength of monochromatized Cu Kα radiation was 0.15418 nm. Raman spectra were recorded on a Horiba LABRAM HR, with a 514 nm excitation laser line. Fourier transform infrared (FTIR) spectra were recorded on a Lambda FTIR-7600 spectrometer over 4000-400 cm^{-1} with a resolution of 4 cm^{-1}. X-ray photoelectron spectroscopy (XPS) measurements were performed at a Thermo Fisher ESCALAB 250Xi XPS microprobe using monochromatic Al Kα radiation (1253.6 eV) as the X-ray source. Morphology and microstructure of the samples were investigated upon a JEOL JEM-2100 F transmission electron microscopy (TEM) under a 200 kV accelerating voltage. Diffuse reflectance spectra (DRS) were measured using a Hitachi U-3010 spectrophotometer fitted with an integrating sphere attachment from 200 to 900 nm with $BaSO_4$ as the reference. Carbon dioxide temperature-programmed desorption (CO_2-TPD) measurements were performed on an Auto Chem II 2920 instrument. Typically, 100 mg of the sample, placed in a glass tube, was pretreated by a He gas flow at 150 °C for 30 min and then cooled down to 50 °C. The adsorption of CO_2 was performed in a CO_2 (10% in He) gas flow at 50 °C for 2 h. After purge by He gas, the sample was heated from 50 to 700 °C at a rate of 10 °C/min. The TPD signal was recorded by a thermal conductivity detector. Electron paramagnetic resonance (EPR) spectra were obtained by a Bruker A30 EPR spectrometer (300 K, 9.866 GHz, X-band). Photoluminescence (PL) spectra were obtained to investigate the ˙OH radicals from a Hitachi F-4600 fluorescence spectrophotometer at room temperature. The ˙OH scavenger of terephthalic acid was mixed with sodium hydroxide to prepare colorless aqueous solution. 25 mg of the catalyst with as prepared solution (terephthalic acid: 0.5 mM, sodium hydroxide: 2 mM) was added into the reactor, then dry nitrogen was bubbled continuously through the suspension in the dark for 40 min, after which the illumination was turned on for 90 min. The peak intensity of FL indicated the concentration of ˙OH radicals in the catalytic system. The fluorescence wavelength which represents the generation of ˙OH is 425 nm with the excitation at 315 nm.

2.3. Photoelectrochemical analysis

Photoelectrochemical analyses were conducted on a Chenhua CHI 660D electrochemical workstation with conventional three-electrode quartz cell system: a platinum sheet and a saturated calomel electrode (SCE) were used as the counter and reference electrodes respectively, while a CHF-XM-500 W Xe-lamp served as light source. To make a working electrode, catalyst powders were deposited on a fluorine-doped tin oxide (FTO) substrate. Typically, a slurry containing 10 mg photocatalysts and 1.0 mL ethanol was made and ultrasonically scattered for several minutes, then 100 μL of the slurry above was coated onto FTO glass. After natural evaporation of ethanol, the working electrodes were then calcined at 120 °C for 2 h in an argon atmosphere to improve the attachment. During the measurements, the electrolyte of 0.1 M Na_2SO_4 solution (pH 6.8) was bubbled with carbon dioxide or Argon.

2.4. Photocatalytic CO_2 reduction

The experiments of gas-phase CO_2 photoreduction with H_2O on photocatalysts were carried out in a closed pyrex cell (600 mL) with a quartz window under 500 W Xe-lamp, while the whole reaction process was maintained at 30 °C. Generally, WO or Mo-WO powder (25 mg) was sprinkled on bottom of the pyrex cell. Water (0.5 mL) was sprayed around the catalyst. Prior to the irradiation, the cell was purged with dry nitrogen, followed by injection of CO_2 (0.25 ml, about 400 ppm). The gaseous products (CO, CH_4) was analyzed by a gas chromatograph (GC, Tianmei 7890) equipped with a TDX-01 column and a flame ionization detector (FID). Some possibly existed by-products were also analyzed. C_2H_6 was analyzed by a gas chromatograph (GC, Tianmei 7890) equipped with a TM-Al_2O_3/S column and a flame ionization detector (FID). Products those can dissolve in water were absorbed into 15 mL water and analyzed by a gas chromatograph (GC, Tianmei 7890) equipped with a SE-54 column and a flame ionization detector (FID). The H_2 product was analyzed by a GC (Tianmei 7890II) equipped with a Molecular Sieve 5 A 80/100 Mesh column and a thermal conductivity detector (TCD).

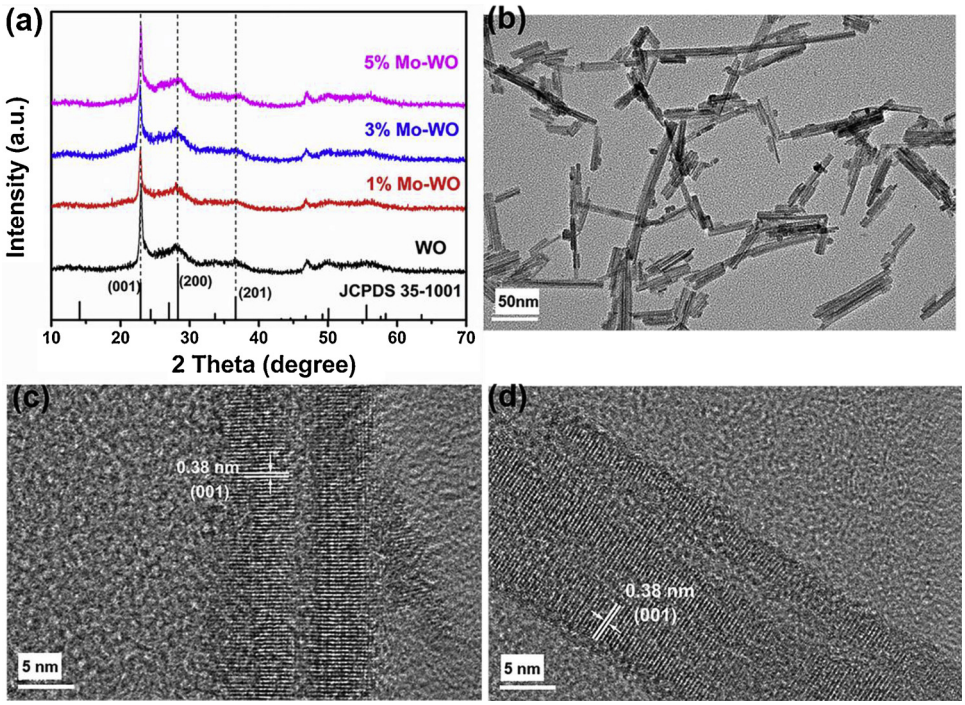

Fig. 1. (a) XRD patterns of WO, 1%Mo-WO, 3%Mo-WO and 5%Mo-WO nanorods, (b) TEM image of 3%Mo-WO, (c) HRTEM image of WO, (d) HRTEM image of 3% Mo-WO nanorods.

3. Results and discussion

3.1. Structure and morphology

Fig. 1a depicts the XRD patterns of $WO_3{\cdot}0.33H_2O$ (noted as WO) and Mo-doped $WO_3{\cdot}0.33H_2O$ (noted as Mo-WO) nanorods with various Mo/W ratios. All of the peaks can be well-indexed to the hexagonal phase of $WO_3{\cdot}0.33H_2O$ (JCPDS 35-1001), similar to a previous report using K_2SO_4 assisted method to fabricate hexagonal WO_3 [38]. The intensity of the (001) plane is stronger than that of the rest of the planes, implying that [001] is the preferential growth direction of WO along the c-axis. The sharp peaks indicate the as-synthesized product is well-crystallized. After doping WO with Mo ions, no new peak appears, indicating the homogeneous doping of Mo into the lattice of WO. Transmission electron microscopy (TEM) images for as-prepared WO and Mo-doped WO samples are shown in Fig. 1b and Fig. S1. WO has a rod-shaped morphology with diameters of 5–10 nm, as well as Mo-doped WO. The HRTEM images of WO and 3%Mo-WO are supplemented in Fig. 1c, d, in which the crystal lattice stripes are clearly demonstrated. The lattice spacing of 0.38 nm is assigned to the (001) planes of $WO_3{\cdot}0.33H_2O$, which indicates that the WO nanorods grow in the [001] direction. This is in agreement with the XRD result that the hexagonal phase of $WO_3{\cdot}0.33H_2O$ has preferential c-orientation. After Mo doping, the lattice spacing hardly changed.

Raman spectra for the as-synthesized WO and Mo-WO nanorods are shown in Fig. 2a, providing further structural composition information. The bands at 253 and 332 cm^{-1} are related to the W—O—W bending modes, while the bands at 759 and 802 cm^{-1} are related to O—W—O stretching modes [39]. The band at around 962 cm^{-1} is assigned to the stretching mode of the terminal W═O bond [40]. This mode is common for all types of tungsten trioxide hydrates. Fig. 2b displays the FTIR spectra of the as-synthesized WO and 3%Mo-WO nanorods. Absorption bands at 560–850 cm^{-1} and 954 cm^{-1} for WO are the characteristics of the stretching modes of O—W—O and W═O, respectively [41]. Minor peaks at 2308–2380 cm^{-1} are ascribed to CO_2 adsorption on WO. Broad absorption band at 3460 cm^{-1} and sharp band at 1634 cm^{-1} have been observed, originating from stretching and bending vibrations of OH group, indicating that the sample contains water molecules [42]. The FTIR spectra exhibit the clean surface of our samples. Furthermore, no distinct position changes of Raman and FTIR spectra could be observed after Mo doping, confirming that doping of WO exerted negligible influence on its structure.

The UV–vis-NIR absorption spectra of the WO and Mo-WO samples are performed in Fig. 3a. A higher broad absorption tail appears in WO, suggesting polaron-to-polaron transitions between W^{6+} and the adjacent W^{5+} or W^{4+} states through hopping induced by incident photons [43,44]. As Mo concentration increases, the absorption intensity in the range of 450–900 nm increases obviously, indicating the enhanced polaron-to-polaron transitions between two adjacent non-equivalent W or Mo sites through hopping. The enhanced polaron-to-polaron transitions may attribute to the developed low valence Mo^{5+} species in our samples which provide new sites for polaron hopping. The intrinsic UV–vis absorption edges of the WO, 1%Mo-WO and 3%Mo-WO (Fig. 3b) are almost the same, indicating a similar intrinsic band gap of about 2.63 eV. However, we notice that excessive Mo doping (> 3 mol %) induces a slight decrease of band gap (2.55 eV), which may be due to creating new defects in the samples.

To further investigate whether the position of the band edges is influenced by Mo doping, electrochemical Mott–Schottky measurements were performed to measure the flat-band potential (E_{fb}) of the WO and 3%Mo-WO. As shown in Fig. 3c and d, the slope of linear $1/C^2$ potential curve is positive, indicating that WO is a characteristic n-type semiconductor. The E_{fb} values are calculated from the intercept of the axis with potential values to be -0.16 and -0.14 V vs. NHE at pH 7 for WO and 3%Mo-WO, respectively. Generally, the position of E_{fb} is considered to be about 0.1 V below the conduction band (E_{cb}) for many n-type semiconductors [12]. As a result, the E_{cb} of WO and 3%Mo-WO is -0.26 and -0.24 V vs. NHE at pH 7, respectively. As seen in Fig. 3e, though the E_{cb} and the valence band (E_{vb}) slightly positively shifted after Mo doping, 3%Mo-WO still met the potential demand for CO_2 reduction to CH_4. In addition, the thermodynamical reduction potential would dramatically decrease by adsorption and activation which may play a more important role in promoting CO_2 reduction [19,20].

In order to shed light on the compositions and elementary valence

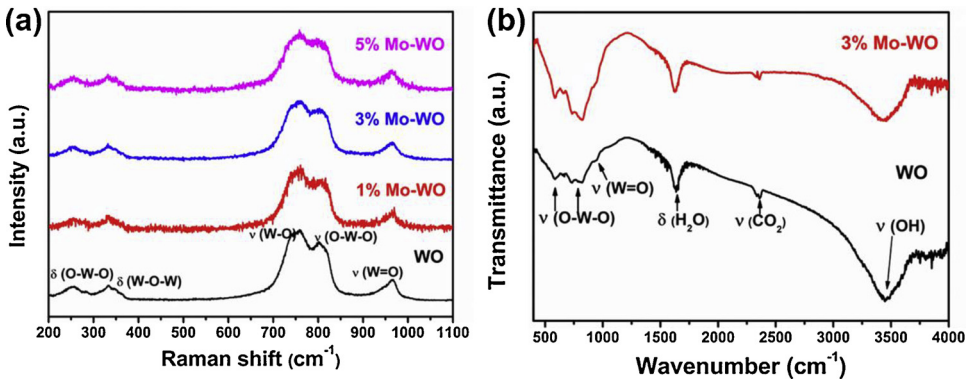

Fig. 2. (a) Raman spectra of WO, 1%Mo-WO, 3%Mo-WO and 5%Mo-WO nanorods, (b) FTIR spectra of WO and 3%Mo-WO nanorods.

states of the samples, X-ray photoelectron spectroscopy (XPS) analysis was then carried out (Fig. S2 and Fig.· 4). As shown in Table S1, the surface Mo/W ratios determined by XPS data is comparable to the chemical composition measured by EDS, indicating a homogeneous distribution of Mo and W in the samples. As displayed in Fig. 4a, the high resolution spectrum of W 4f presents two strong peaks at 37.6 eV and 35.5 eV for WO sample, which could be severally assigned to W $4f_{5/2}$ and W $4f_{7/2}$ of W^{6+}, while two minor peaks at 36.7 eV and 34.6 eV can be ascribed to W^{5+} [31]. The co-existence of W^{6+} and W^{5+} confirms polaron-to-polaron transitions in our samples, fairly agreeing with the broad absorption tail in UV–vis-NIR absorption spectra in Fig. 3a.

Fig.4b shows O 1 s XPS spectra of the samples. The peak at 530.5 eV is ascribed to the lattice oxygen, while the other two peaks located at 531.4 and 533.3 eV are attributed to the O-atoms in the surface OH and

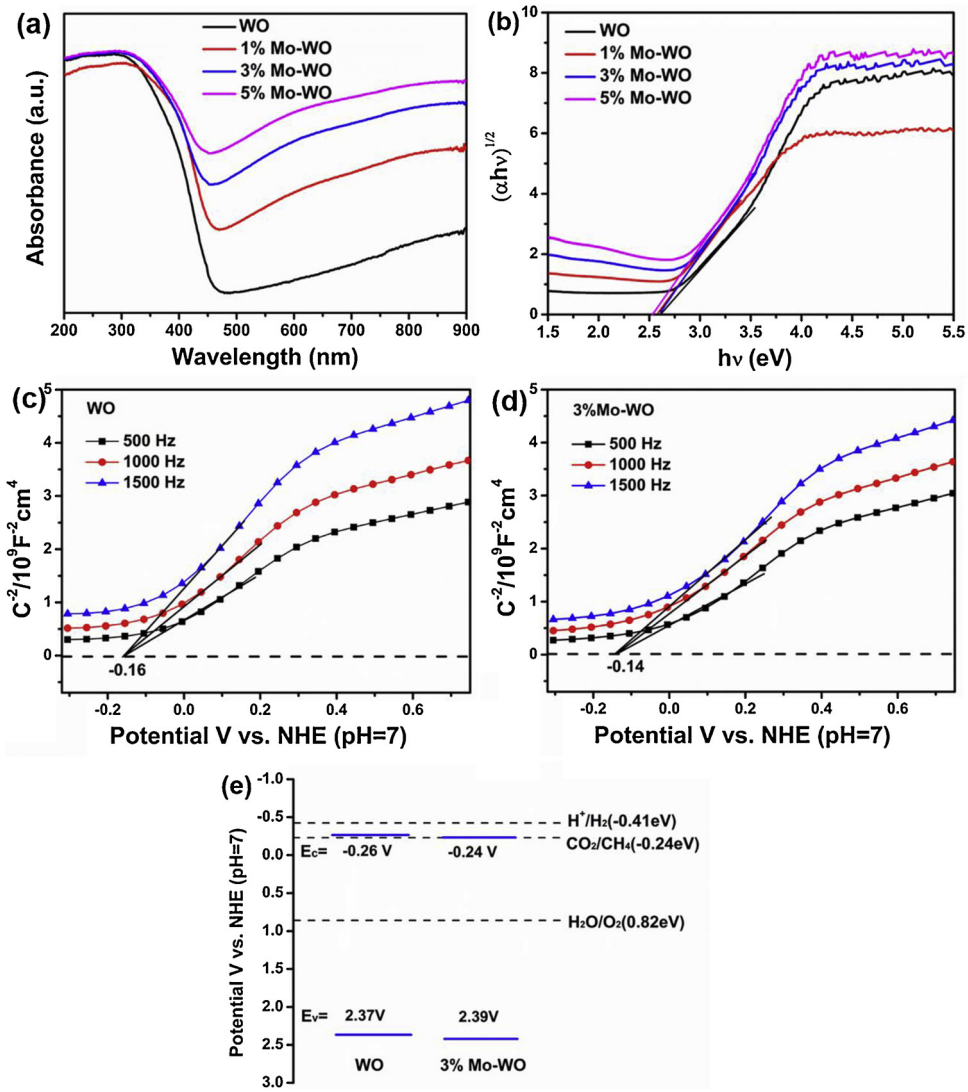

Fig. 3. (a) Ultraviolet-visible-near infrared (UV–vis-NIR) absorption spectra and (b) plots of transformed Kubelka-Munk function versus photon energy for WO, 1% Mo-WO, 3%Mo-WO and 5%Mo-WO nanorods; Mott-Schottky plots of WO (c) and 3%Mo-WO (d); (c) band structure alignments of WO and 3%Mo-WO.

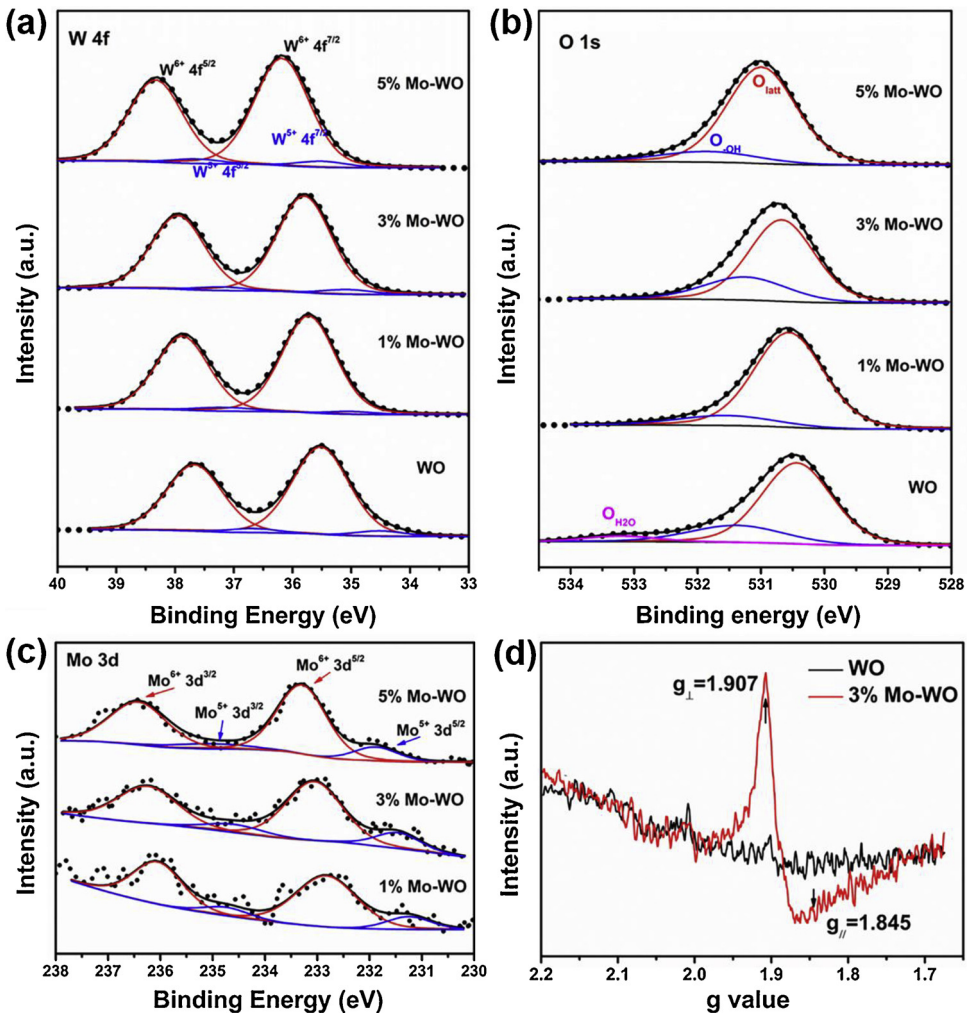

Fig. 4. XPS spectra of W 4f (a), O 1 s (b), and Mo 3d (c) for WO, 1%Mo-WO, 3%Mo-WO and 5%Mo-WO nanorods; (d) EPR spectra at 300 K for WO and 3%Mo-WO.

the O-atoms in the surface OH_2, respectively [12,45]. The high-resolution Mo 3d XPS spectrum of 3%Mo-WO (Fig. 4c) reveals that both Mo^{6+} (binding energy at 232.9 and 236.2 eV) and Mo^{5+} (binding energy at 231.3 and 234.51 eV) are presented in the samples [31]. The introduction of Mo^{5+} enhances polaron-to-polaron transitions and improves the ability to harvest vis-NIR light (Fig. 3a). For Mo-doped WO, the characteristic peaks of W 4f and O 1 s were shifted to higher binding energy with increasing the concentration of Mo, which indicates the electronic modulation of WO by Mo doping.

EPR spectra are further used to determine the low valence state metal ions in our samples. The spectra are similar with that of the recent report [32]. According to Fig. 4d, a hyperfine structure with both parallel ($g_{//}$ = 1.846) and perpendicular ($g_{\perp}$ = 1.907) bands relevant to Mo species occurs in the EPR spectrum of Mo-WO, which indicates the existence of Mo—O tetragonal pyramids [32]. The penta-coordination further proves the presence of coordinately unsaturated Mo species in Mo-WO [32]. According to previous reports, owing to the strong electron donating power, low-valent metal species such as Ti^{3+} and Bi^{2+} give good CO_2 or N_2 activation performance [46–49]. Therefore, Mo^{5+} and W^{5+} species in our sample may also promote CO_2 activation.

3.2. Photocatalytic activity

To assess the catalytic performance, photocatalytic CO_2 reduction was conducted at room temperature and atmospheric pressure. Firstly, no organics were used as raw materials in our samples, excluding the possible influence of other carbon sources. Besides, a control experiment was carried out without either photocatalysts or illumination, no detectable products were observed, indicating that both the photocatalysts and light irradiation are indispensable for CO_2 photoreduction. It is worth noting that no H_2, C_2H_6, methanol or ethanol was detected during the photocatalytic process (Fig. S3, S4). Fig. 5 summarizes the photocatalytic CO_2 reduction activity of the WO and Mo-WO samples. As depicted in Fig. 5a, the 3%Mo-WO sample exhibits the highest performance for the photocatalytic CO_2 reduction to CH_4 (31.8 umol g^{-1}) during the first six hours under atmospheric CO_2 concentration (400 ppm), which is about 5.2 times higher than that of WO (6.1 umol g^{-1}) under the same conditions, indicating the superior effect of Mo doping in WO. However, the change of CO yield is slightly relevant to Mo doping (Fig. S5). For 3%Mo-WO sample, the CO productive rate is only about 1.2 times higher than that of WO, demonstrating Mo doping mainly improves the activity of CH_4 generation. As shown in Fig. 5b, the CH_4 selectivity is highly improved from 27.3% to 61.2% after Mo doping, among which 3%Mo-WO reaches the highest selectivity. In addition, the yields of CH_4 production were acceptably stable in at least 5 cycles, indicating the stability of 3%Mo-WO catalyst (Fig. 5c).

3.3. Mechanism and discussion

Mo doping in WO has highly improved the activity of CO_2 photoreduction, especially for CH_4 generation. To better understand the process and guide our future works, the roles of Mo doping in CO_2 activation and protonation should be investigated carefully.

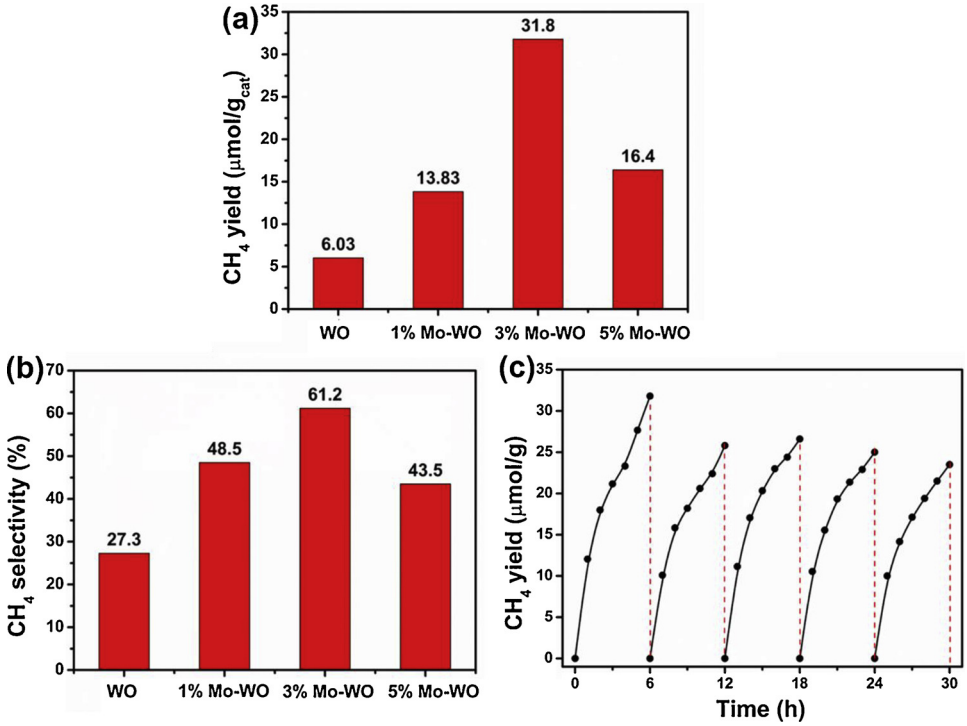

Fig. 5. The yield (a) and selectivity (b) of photocatalytic CO_2 reduction to CH_4 in the first 6 h for WO, 1%Mo-WO, 3%Mo-WO and 5%Mo-WO, (selectivity of CH_4 = $[8n(CH_4)] / [2n(CO) + 8n(CH_4) + 2n(H_2)] \times 100$); (c) Cycling curves of CH_4 yield for 3%Mo-WO.

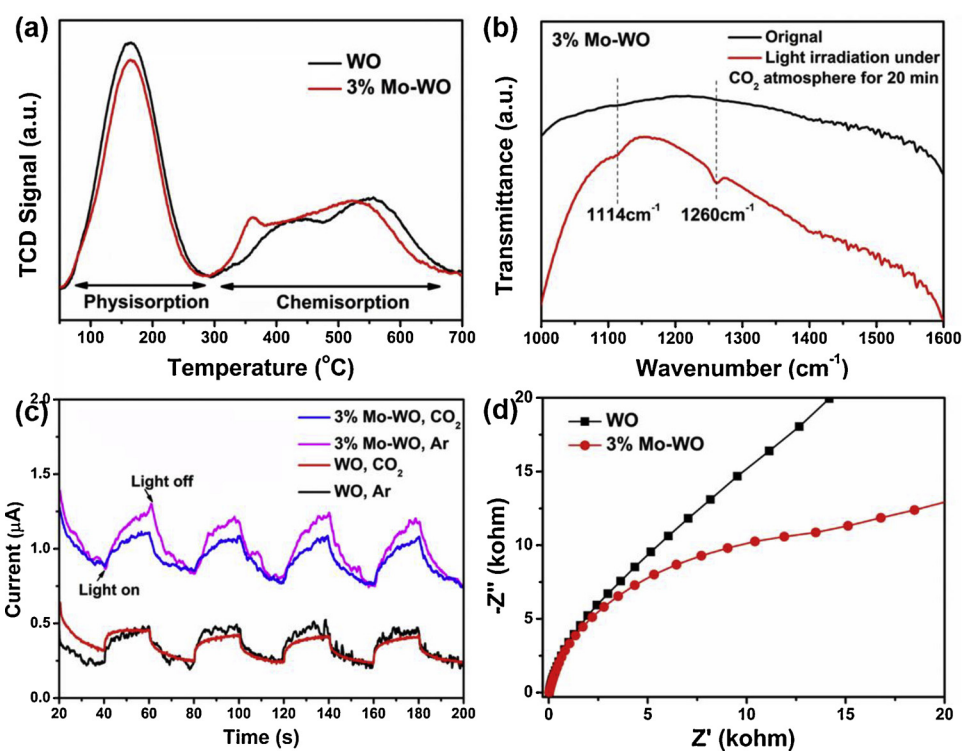

Fig. 6. (a) CO_2 TPD curves for WO and 3%Mo-WO; (b) FTIR spectra at 1000-1600 cm^{-1} of 3% Mo-WO before (black line) and after (red line) light irradiation under CO_2 atmosphere; (c) Transient photocurrent responses of WO and 3%Mo-WO in CO_2 or Ar atmosphere; (d) EIS Nyquist plots of WO and 3%Mo-WO (For interpretation of the references to colour in this figure legend, the reader is referred to the web version of this article.).

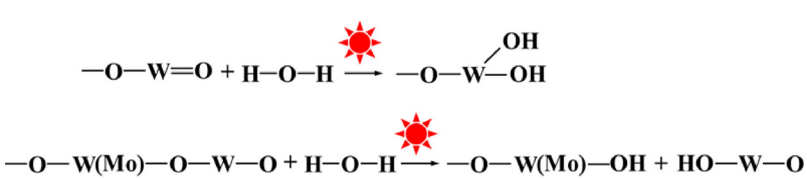

Scheme 1. Schematic illustration of the water splitting in the WO or Mo-WO by light excitation.

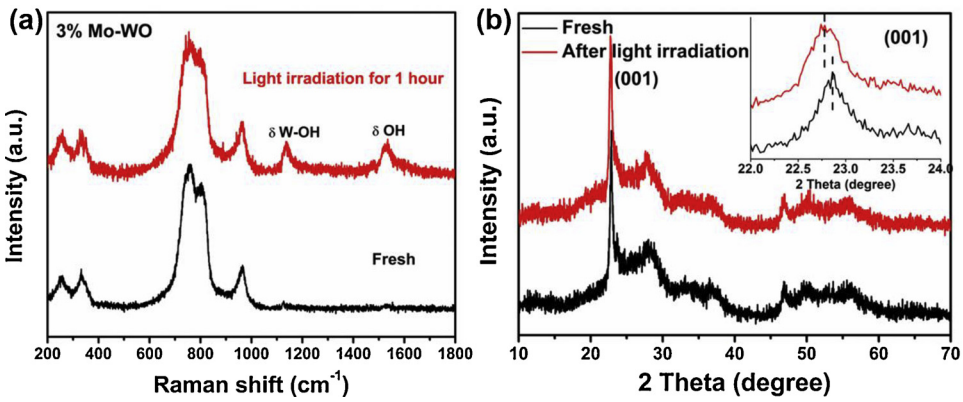

Fig. 7. (a) Raman spectra of 3%Mo-WO before (black line) and after (red line) light irradiation for 1 h under reaction system; (b) XRD patterns of 3%Mo-WO before (black line) and after (red line) light irradiation (For interpretation of the references to colour in this figure legend, the reader is referred to the web version of this article.).

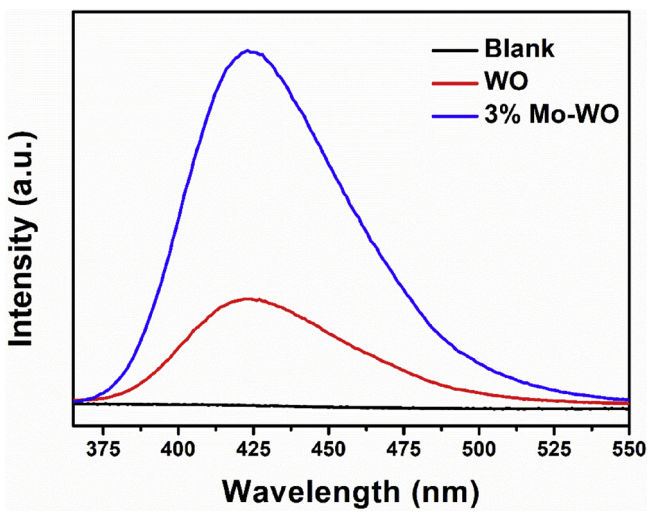

Fig. 8. The FL spectra for the generation of ˙OH in an aqueous solution by photocatalytic water oxidation through WO or 3%Mo-WO in 90 min.

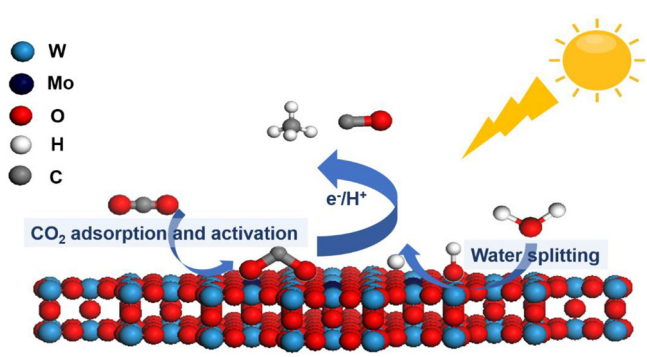

Scheme 2. Photocatalytic CO_2 reduction over Mo-WO with water under solar irradiation.

3.3.1. CO_2 activation

Considering the thermodynamical stability of CO_2, the adsorption and activation of CO_2 are supposed to be discussed. Firstly, the CO_2 temperature-programmed desorption (TPD) has been carried out to reveal the adsorption sites of CO_2 on the surface of WO and Mo-doped WO samples. As shown in Fig. 6a, the TPD profiles contains three major desorption peaks. A low-temperature desorption peak occurs at approximately 160 °C due to physical adsorption, assigned to the linear adsorbed CO_2 by surface OH [12]. The medium-temperature desorption peaks between 280 °C and 450 °C is most likely associated with the lattice oxygen anions, while the peak above 450 °C probably corresponds to the CO_2 desorption on the strong basic sites of low-coordination oxygen [50]. In view of the above, it is found that both of the WO and Mo-WO have great ability for CO_2 adsorption, and the CO_2 adsorption capacity is similar.

To further examine the adsorption and chemical activation of CO_2 molecule on the WO and Mo-WO, FTIR spectra were displayed in Fig. 6b and Fig. S6. The weak IR bands at 1410–1490 and 1500–1590 cm^{-1} may be assign to the bicarbonate (HCO_3^-) features and mono- and bidentate carbonates (b-CO_3^{2-}, m-CO_3^{2-}), respectively, which was induced by exposing the WO and Mo-WO to air or CO_2 atmosphere [51]. After light irradiation under CO_2 atmosphere for 20 min, the key intermediates of CO_2^- species at 1260 cm^{-1} were observed [19,52]. This finding suggests that the surface active sites of Mo-WO can trap the photogenerated electrons and then effectively facilitate the process of electron injection to the adsorbed CO_2 molecules, achieving the CO_2 activation. Normally, the one-electron reduction of CO_2 is very difficult, but the literatures have reported that the single-electron reduction of CO_2 to CO_2^- easily occurred on low-valent metal species such as Ti^{3+} and Bi [9,21,53]. This suggests that the W^{5+} and Mo^{5+} in our samples promote the one-electron transfer reaction.

To further look into the role of Mo doping for CO_2 activation, photoelectrochemical method was conducted to examine the interfacial charge kinetics for WO and Mo-WO through transient photocurrent responses in different atmosphere. In Fig. 6c, the photocurrent in Ar atmosphere can be ascribed to the transfer of photo-induced electrons to electrode, while in CO_2 saturated solution, photocurrent would compete with electrons transfer to CO_2 [32]. Intriguingly, the photocurrent density of 3%Mo-WO under the CO_2 atmosphere reduces about 30% than that under the Ar atmosphere, while for WO, the photocurrent density reduces 21%, indicative of the stronger interaction between the surface active sites and CO_2 for 3%Mo-WO. Mo doping is highly favorable for the interfacial electrons transfer from the excited Mo-WO to the adsorbed CO_2, promoting photocatalytic CO_2 activation and reduction. In addition, similar to the report, WO and Mo-WO have the ability to store photogenerated electrons with enhanced vis-NIR absorption under light irradiation (Fig. S7) [54]. To compare the electrons storage and release ability, the transient photocurrent of WO and Mo-WO after light irradiation for one hour are displayed in Fig. S8. The transient current of 3%Mo-WO (Fig. S8) exhibits obvious charge release once the light is shielded, indicating sufficient charge storage on exposure to photons [55]. In comparison with the signal of pristine WO, the above charge storage and release should be reasonably attributed to that the Mo doping improves the electrons storage and localization ability. It is supposed that Mo^{5+} ions doped in WO prefer to localize electrons around them and enhance photo-induced electron density on the active sites, so as to improving the electron-giving ability for CO_2 activation and reduction. Besides, a smaller semicircle for the Mo doping sample from Nyquist plots (Fig. 6d) points out a lower resistance, which is also beneficial to interfacial electrons transfer and CO_2 photoreduction.

3.3.2. Water splitting and proton/electron insertion

In addition to the surface CO_2 activation, photoinduced protonation with electron/proton transfer is another elementary step for CO_2 reduction to CH_4. Water splitting ($H_2O \rightarrow OH_{ads} + x\ H^+ + x\ e^-$) followed by proton and electron insertion reaction under light irradiation ($WO + x\ H^+ + x\ e^- \rightarrow H_xWO$) which converts WO into tungsten bronze (H_xWO, $0 < x < 1$), was observed in Mo-WO and WO [56–58]. Protons and electrons are inserted into the lattice of WO or Mo-WO and stabilized as Brønsted acidic OH groups and W^{5+} or Mo^{5+} sites, respectively, acting as active sites for the hydrogenation reaction [24,59–63]. Hence proton insertion process guaranteed the supply of required electrons and protons for the hydrogenation process of the activated CO_2 to generate CH_4. The water splitting and proton insertion process can be exhibited by the following reaction schemes (Scheme 1), which has been evidenced by Raman spectra (Fig. 7a and Fig. S9), XRD (Fig. 7b) and FTIR spectra (Fig. 6b). As shown in Fig. 7a, after the Mo-WO was irradiated by Xe-lamp under water vapor atmosphere, the new strong peaks appeared at 1135 and 1538 cm^{-1}, corresponding to the bending vibration of the W—OH and O—H in W—OH bond, which is due to the surface adsorbed water spitting and proton bonding with lattice atoms by proton insertion reaction [40,62]. In Fig. 6b, the peak appearing at 1114 cm^{-1} after light irradiation is also assigned to the bending vibration of the W—OH, agreeing with the Raman spectra [41]. Fig. 7b shows the evolution of (001) reflections after light irradiation. With proton insertion, the (001) peak moves to lower two-theta direction, suggesting an extended (001) lattice space with proton insertion, which coincides with previous reports [55,63].

Obviously, the efficiency of proton generation and insertion for CO_2 reduction plays a great role in promoting CH_4 generation, which is usually limited by water oxidation step. Due to the reaction ($H_2O + h^+ \rightarrow H^+ + {}^{\cdot}OH$) could happen in aqueous solution by photocatalytic water oxidation through WO, the amount of ˙OH is used to assess the water oxidation ability of catalysts [64]. The photocatalytic activities toward water oxidation were evaluated in aqueous solution containing terephthalic acid (0.5 mM) as the ˙OH scavenger. Fig. 8 shows the FL spectra for the generation of ˙OH in an aqueous solution by photocatalytic water oxidation through WO or 3%Mo-WO in 90 min. The peak intensity of FL indicated the concentration of ˙OH radicals in the aqueous solution. Mo-WO displays a higher rate of ˙OH evolution compared with WO, illustrating the property of Mo doping for boosting water oxidation. Furthermore, the enhanced water oxidation increases the efficiency of proton generation, and then promoting proton insertion and conduction to react with CO_2 intermediate to generate CH_4.

Based on the above results, the photocatalytic CO_2 reduction process over Mo-WO can be illustrated as Scheme 2. Generally, CO_2 adsorption on the Mo-WO leads to the formation of a partially charged species ${CO_2}^{\delta-}$ which is bended and activated on the surface. Meanwhile, water is dissociated into protons and hydroxyls followed by proton insertion and conduction in the lattice of Mo-WO. Subsequently, the photogenerated electrons coupled with the protons react with the activated ${CO_2}^{\delta-}$ species. Mo doping highly boosts the transfer efficiency of electrons and protons to the reaction sites. As a result, the enhanced photocatalytic CO_2 reduction to CH_4 is achieved, while some CO is also generated in this process.

4. Conclusion

In summary, Mo-doped WO nanorods with diameter of 5–10 nm were synthesized by hydrothermal method. The 3%Mo-WO nanorods realize photocatalytic CO_2 reduction into CH_4 with a rate of 5.3 μmol ${g_{cat}}^{-1}h^{-1}$ under atmospheric CO_2 concentration (about 400 ppm), which is about 5.2 times higher than that of pristine WO. The Mo doping in the WO nanorods improves the electrons storage and localization ability, enhancing photo-induced electron density in the active sites, which could highly boost the transfer of photoexcited electrons to adsorbed CO_2, thereby facilitating CO_2 activation and reduction. In addition, proton and electron insertion converts WO into tungsten bronze (H_xWO), guaranteeing required electrons and protons for CO_2 reduction. The enhanced water oxidation of Mo-doped WO promotes proton supply and insertion process, improving the hydrogenation process of the carbon intermediate to generate CH_4. The combined action of the enhanced CO_2 activation and water oxidation with efficient proton and electron insertion improves the performance of CO_2 photoreduction to CH_4. This work provides a strategy for regulating active sites via a simple doping strategy to promote photocatalytic CO_2 reduction.

Acknowledgment

This work was financially supported by the National Natural Science Foundation of China (51772312, 51472260).

Appendix A. Supplementary data

Supplementary material related to this article can be found, in the online version, at doi:https://doi.org/10.1016/j.apcatb.2018.11.021.

References

[1] J.K. Stolarczyk, S. Bhattacharyya, L. Polavarapu, J. Feldmann, Challenges and prospects in solar water splitting and CO_2 reduction with inorganic and hybrid nanostructures, ACS Catal. 8 (2018) 3602–3635.
[2] A.M. Appel, J.E. Bercaw, A.B. Bocarsly, H. Dobbek, D.L. DuBois, M. Dupuis, J.G. Ferry, E. Fujita, R. Hille, P.J. Kenis, C.A. Kerfeld, R.H. Morris, C.H. Peden, A.R. Portis, S.W. Ragsdale, T.B. Rauchfuss, J.N. Reek, L.C. Seefeldt, R.K. Thauer, G.L. Waldrop, Frontiers, opportunities, and challenges in biochemical and chemical catalysis of CO_2 fixation, Chem. Rev. 113 (2013) 6621–6658.
[3] X. Liu, S. Inagaki, J. Gong, Heterogeneous molecular systems for photocatalytic CO_2 reduction with water oxidation, Angew. Chem., Int. Ed. 55 (2016) 14924–14950.
[4] Nathan S. Lewis, D.G. Nocera, Powering the planet: chemical challenges in solar energy utilization, Proc. Natl. Acad. Sci. U. S. A. 103 (2006) 15729–15735.
[5] C. Dong, C. Lian, S. Hu, Z. Deng, J. Gong, M. Li, H. Liu, M. Xing, J. Zhang, Size-dependent activity and selectivity of carbon dioxide photocatalytic reduction over platinum nanoparticles, Nat. Commun. 9 (2018) 1252.
[6] C. Dong, M. Xing, J. Zhang, Economic hydrophobicity triggering of CO_2 photoreduction for selective CH_4 generation on noble-metal-free TiO_2-SiO_2, J. Phys. Chem. Lett. 7 (2016) 2962–2966.
[7] S.N. Habisreutinger, L. Schmidt-Mende, J.K. Stolarczyk, Photocatalytic reduction of CO_2 on TiO_2 and other semiconductors, Angew. Chem., Int. Ed. 52 (2013) 7372–7408.
[8] X. Chang, T. Wang, J. Gong, CO_2 photo-reduction: Insights into CO_2 activation and reaction on surfaces of photocatalysts, Energy Environ. Sci. 9 (2016) 2177–2196.
[9] V.P. Indrakanti, J.D. Kubicki, H.H. Schobert, Photoinduced activation of CO_2 on Ti-based heterogeneous catalysts: current state, chemical physics-based insights and outlook, Energy Environ. Sci. 2 (2009) 745–758.
[10] W. Zhang, L. Wang, H. Liu, Y. Hao, H. Li, M.U. Khan, J. Zeng, Integration of quantum confinement and alloy effect to modulate electronic properties of RhW nanocrystals for improved catalytic performance toward CO_2 hydrogenation, Nano Lett. 17 (2017) 788–793.
[11] M.U. Khan, L. Wang, Z. Liu, Z. Gao, S. Wang, H. Li, W. Zhang, M. Wang, Z. Wang, C. Ma, J. Zeng, Pt_3Co octapods as superior catalysts of CO_2 hydrogenation, Angew. Chem., Int. Ed. 55 (2016) 9548–9552.
[12] S. Sun, M. Watanabe, J. Wu, Q. An, T. Ishihara, Ultrathin $WO_3 \cdot 0.33H_2O$ nanotubes for CO_2 photoreduction to acetate with high selectivity, J. Am. Chem. Soc. 140 (2018) 6474–6482.
[13] J. Ran, M. Jaroniec, S.Z. Qiao, Cocatalysts in semiconductor-based photocatalytic CO_2 reduction: achievements, challenges, and opportunities, Adv. Mater. 30 (2018) 1704649.
[14] Y. Kim, J.G. Smith, P.K. Jain, Harvesting multiple electron-hole pairs generated through plasmonic excitation of Au nanoparticles, Nat. Chem. 10 (2018) 763–769.
[15] Z. Xiong, Z. Lei, C.-C. Kuang, X. Chen, B. Gong, Y. Zhao, J. Zhang, C. Zheng, J.C.S. Wu, Selective photocatalytic reduction of CO_2 into CH_4 over Pt-Cu_2O TiO_2 nanocrystals: the interaction between Pt and Cu_2O cocatalysts, Appl. Catal. B-Environ. 202 (2017) 695–703.
[16] C. Dong, S. Hu, M. Xing, J. Zhang, Enhanced photocatalytic CO_2 reduction to CH_4 over separated dual co-catalysts Au and RuO_2, Nanotechnology 29 (2018) 154005.
[17] C. Dong, M. Xing, J. Zhang, Double-cocatalysts promote charge separation efficiency in CO_2 photoreduction: spatial location matters, Mater. Horiz. 3 (2016) 608–612.
[18] G. Xi, S. Ouyang, P. Li, J. Ye, Q. Ma, N. Su, H. Bai, C. Wang, Ultrathin $W_{18}O_{49}$ nanowires with diameters below 1 nm: synthesis, near-Infrared absorption, photoluminescence, and photochemical reduction of carbon dioxide, Angew. Chem., Int. Ed. 51 (2012) 2395–2399.
[19] J. Wu, X. Li, W. Shi, P. Ling, Y. Sun, X. Jiao, S. Gao, L. Liang, J. Xu, W. Yan, C. Wang, Y. Xie, Efficient visible-light-driven CO_2 reduction mediated by defect-

engineered BiOBr atomic layers, Angew. Chem., Int. Ed. 57 (2018) 8719–8723.
[20] Z. Geng, X. Kong, W. Chen, H. Su, Y. Liu, F. Cai, G. Wang, J. Zeng, Oxygen vacancies in ZnO nanosheets enhance CO_2 electrochemical reduction to CO, Angew. Chem., Int. Ed. 57 (2018) 6054–6059.
[21] G. Yin, X. Huang, T. Chen, W. Zhao, Q. Bi, J. Xu, Y. Han, F. Huang, Hydrogenated blue titania for efficient solar to chemical conversions: preparation, characterization, and reaction mechanism of CO_2 reduction, ACS Catal. 8 (2018) 1009–1017.
[22] Y. Zhao, G. Chen, T. Bian, C. Zhou, G.I. Waterhouse, L.Z. Wu, C.H. Tung, L.J. Smith, D. O'Hare, T. Zhang, Defect-rich ultrathin ZnAl-layered double hydroxide nanosheets for efficient photoreduction of CO_2 to CO with water, Adv. Mater. 27 (2015) 7824–7831.
[23] L. Liang, X. Li, Y. Sun, Y. Tan, X. Jiao, H. Ju, Z. Qi, J. Zhu, Y. Xie, Infrared light-driven CO2 overall splitting at room temperature, Joule 2 (2018) 1004–1016.
[24] Y.F. Li, N. Soheilnia, M. Greiner, U. Ulmer, T. Wood, A.A. Jelle, Y. Dong, A.P. Yin Wong, J. Jia, G.A. Ozin, Pd@H_yWO_{3-x} nanowires efficiently catalyze the CO_2 heterogeneous reduction reaction with a pronounced light effect, ACS Appl. Mater. Inter. (2018), https://doi.org/10.1021/acsami.8b04982.
[25] L. Wang, Y. Wang, Y. Cheng, Z. Liu, Q. Guo, M.N. Ha, Z. Zhao, Hydrogen-treated mesoporous WO_3 as a reducing agent of CO_2 to fuels (CH_4 and CH_3OH) with enhanced photothermal catalytic performance, J. Mater. Chem. A 4 (2016) 5314–5322.
[26] M. Shi, X. Tong, W. Li, J. Fang, L. Chen, C.A. Ma, Enhanced electrocatalytic oxygen reduction on $NiWO_x$ solid solution with induced oxygen defects, ACS Appl. Mater. Inter. 9 (2017) 34990–35000.
[27] Z. Xiong, Z. Lei, S. Ma, X. Chen, B. Gong, Y. Zhao, J. Zhang, C. Zheng, J.C.S. Wu, Photocatalytic CO_2 reduction over V and W codoped TiO_2 catalyst in an internal-illuminated honeycomb photoreactor under simulated sunlight irradiation, Appl. Catal. B- Environ. 219 (2017) 412–424.
[28] Y. Chen, Z. Dong, Z. Huang, M. Zhou, J. Gao, J. Chen, C. Li, Z. Ma, J. Chen, X. Tang, Tuning electronic states of catalytic sites enhances SCR activity of hexagonal WO_3 by Mo framework substitution, Catal. Sci. Technol. 7 (2017) 2467–2473.
[29] P. Bhavani, D. Praveen Kumar, S. Jeong, E.H. Kim, H. Park, S. Hong, M. Gopannagari, D. Amaranatha Reddy, J.K. Song, T.K. Kim, Multidirectional-charge-transfer urchin-type Mo-doped $W_{18}O_{49}$ nanostructures on CdS nanorods for enhanced photocatalytic hydrogen evolution, Catal. Sci. Technol. 8 (2018) 1880–1891.
[30] X. Zhong, Y. Sun, X. Chen, G. Zhuang, X. Li, J.-G. Wang, Mo Doping induced more active sites in urchin-like $W_{18}O_{49}$ nanostructure with remarkably enhanced performance for hydrogen evolution reaction, Adv. Funct. Mater. 26 (2016) 5778–5786.
[31] L. Zhou, J. Zhu, M. Yu, X. Huang, Z. Li, Y. Wang, C. Yu, $Mo_xW_{1-x}O_3 \cdot 0.33H_2O$ solid solutions with tunable band gaps, J. Phys. Chem. C 114 (2010) 20947–20954.
[32] N. Zhang, A. Jalil, D. Wu, S. Chen, Y. Liu, C. Gao, W. Ye, Z. Qi, H. Ju, C. Wang, X. Wu, L. Song, J. Zhu, Y. Xiong, Refining defect states in $W_{18}O_{49}$ by Mo doping: a strategy for tuning N_2 activation towards solar-driven nitrogen fixation, J. Am. Chem. Soc. 140 (2018) 9434–9443.
[33] J. Song, Z.-F. Huang, L. Pan, J.-J. Zou, X. Zhang, L. Wang, Oxygen-deficient tungsten oxide as versatile and efficient hydrogenation catalyst, ACS Catal. 5 (2015) 6594–6599.
[34] T.J. Thibodeau, A.S. Canney, W.J. DeSisto, M.C. Wheeler, F.G. Amar, B.G. Frederick, Composition of tungsten oxide bronzes active for hydrodeoxygenation, Appl. Catal. A- Gen. 388 (2010) 86–95.
[35] X. Li, W. Wang, D. Jiang, S. Sun, L. Zhang, X. Sun, Efficient solar-driven nitrogen fixation over carbon–tungstic acid hybrids, Chem. Eur. J. 22 (2016) 13819–13822.
[36] X.W. Lou, H.C. Zeng, An inorganic route for controlled synthesis of $W_{18}O_{49}$ nanorods and nanofibers in solution, Inorg. Chem. 42 (2003) 6169–6171.
[37] D.M. Kabtamu, J.Y. Chen, Y.C. Chang, C.H. Wang, Electrocatalytic activity of Nb-doped hexagonal WO_3 nanowire-modified graphite felt as a positive electrode for vanadium redox flow batteries, J. Mater. Chem. A 4 (2016) 11472–11480.
[38] X.C. Song, Y.F. Zheng, E. Yang, Y. Wang, Large-scale hydrothermal synthesis of WO_3 nanowires in the presence of K_2SO_4, Mater. Lett. 61 (2007) 3904–3908.
[39] C. Lian, X. Xiao, Z. Chen, Y. Liu, E. Zhao, D. Wang, C. Chen, Preparation of hexagonal ultrathin WO_3 nano-ribbons and their electrochemical performance as an anode material in lithium ion batteries, Nano Res. 9 (2015) 435–441.
[40] R.F. Garcia-Sanchez, T. Ahmido, D. Casimir, S. Baliga, P. Misra, Thermal effects associated with the Raman spectroscopy of WO_3 gas-sensor materials, J. Phys. Chem. A 117 (2013) 13825–13831.
[41] Bridget Ingham, Shen V. Chong, J.L. Tallon, Layered tungsten oxide-based organic-inorganic hybrid materials: an Infrared and Raman study, J. Phys. Chem. B 109 (2005) 4936–4940.
[42] A.K. Nayak, S. Lee, Y.I. Choi, H.J. Yoon, Y. Sohn, D. Pradhan, Crystal phase and size-controlled synthesis of tungsten trioxide hydrate nanoplates at room temperature: enhanced Cr (VI) photoreduction and methylene blue adsorption properties, ACS Sustainable Chem. Eng. 5 (2017) 2741–2750.
[43] S. Cong, F. Geng, Z. Zhao, Tungsten oxide materials for optoelectronic applications, Adv. Mater. 28 (2016) 10518–10528.
[44] S.K. Deb, Opportunities and challenges in science and technology of WO_3 for electrochromic and related applications, Sol. Energy Mater. Sol. C. 92 (2008) 245–258.
[45] Y. Lu, J. Zhang, F. Wang, X. Chen, Z. Feng, C. Li, K_2SO_4-assisted hexagonal/monoclinic WO_3 phase junction for efficient photocatalytic degradation of RhB, ACS Appl. Energy Mater. 1 (2018) 2067–2077.
[46] C. Yang, Y. Yu, B. Linden, J.C.S. Wu, G. Mul, Artificial photosynthesis over crystalline TiO_2-based catalysts: fact or fiction? J. Am. Chem. Soc. 132 (2010) 8398–8406.
[47] Z. Wang, C. Yang, T. Lin, H. Yin, P. Chen, D. Wan, F. Xu, F. Huang, J. Lin, X. Xie, M. Jiang, H-Doped black titania with very high solar absorption and excellent photocatalysis enhanced by localized surface plasmon resonance, Adv. Funct. Mater. 23 (2013) 5444–5450.
[48] S. Sun, Q. An, W. Wang, L. Zhang, J. Liu, W.A. Goddard Iii, Efficient photocatalytic reduction of dinitrogen to ammonia on bismuth monoxide quantum dots, J. Mater. Chem. A 5 (2017) 201–209.
[49] M. Xing, Y. Zhou, C. Dong, L. Cai, L. Zeng, B. Shen, L. Pan, C. Dong, Y. Chai, J. Zhang, Y. Yin, Modulation of the reduction potential of TiO_{2-x} by fluorination for efficient and selective CH_4 generation from CO_2 photoreduction, Nano Lett. 18 (2018) 3384–3390.
[50] K. Wang, L. Zhang, Y. Su, S. Sun, Q. Wang, H. Wang, W. Wang, Boosted CO_2 photoreduction to methane via Co doping in bismuth vanadate atomic layers, Catal. Sci. Technol. 8 (2018) 3115–3122.
[51] L. Zhang, W. Wang, D. Jiang, E. Gao, S. Sun, Photoreduction of CO_2 on BiOCl nanoplates with the assistance of photoinduced oxygen vacancies, Nano Res. 8 (2014) 821–831.
[52] Y. Wang, J. Zhao, T. Wang, Y. Li, X. Li, J. Yin, C. Wang, CO_2 photoreduction with H_2O vapor on highly dispersed CeO_2/TiO_2 catalysts: surface species and their reactivity, J. Catal. 337 (2016) 293–302.
[53] J. Lee, D.C. Sorescu, X. Deng, Electron-induced dissociation of CO_2 on TiO_2(110), J. Am. Chem. Soc. 133 (2011) 10066–10069.
[54] D. Zhao, C. Chen, C. Yu, W. Ma, J. Zhao, Photoinduced electron storage in WO_3/TiO_2 nanohybrid material in the presence of oxygen and postirradiated reduction of heavy metal ions, J. Phys. Chem. C 113 (2009) 13160–13165.
[55] D. Jiang, W. Wang, S. Sun, L. Zhang, Y. Zheng, Equilibrating the plasmonic and catalytic roles of metallic nanostructures in photocatalytic oxidation over Au-modified CeO_2, ACS Catal. 5 (2014) 613–621.
[56] Z. Chen, Y. Peng, F. Liu, Z. Le, J. Zhu, G. Shen, D. Zhang, M. Wen, S. Xiao, C.P. Liu, Y. Lu, H. Li, Hierarchical nanostructured WO_3 with biomimetic proton channels and mixed ionic-electronic conductivity for electrochemical energy storage, Nano Lett. 15 (2015) 6802–6808.
[57] M.F. Daniel, B. Desbat, J.C. Lassegues, Infrared and Raman spectroscopies oxide films of rf sputtered tungsten oxide films, J. Solid State Chem. 73 (1988) 127–139.
[58] A.C.C. Tseung, K.Y. Chen, Hydrogen spill-over effect on Pt/WO_3 anode catalysts, Catal. Today 38 (1997) 439–443.
[59] J. An, Y. Wang, J. Lu, J. Zhang, Z. Zhang, S. Xu, X. Liu, T. Zhang, M. Gocyla, M. Heggen, R.E. Dunin-Borkowski, P. Fornasiero, F. Wang, Acid-promoter-free ethylene methoxycarbonylation over Ru-clusters/ceria: the catalysis of interfacial Lewis acid-base pair, J. Am. Chem. Soc. 140 (2018) 4172–4181.
[60] Y. Peng, L. Wang, Q. Luo, Y. Cao, Y. Dai, Z. Li, H. Li, X. Zheng, W. Yan, J. Yang, J. Zeng, Molecular-level insight into how hydroxyl groups boost catalytic activity in CO_2 hydrogenation into methanol, Chem 4 (2018) 613–625.
[61] X. Li, H. Pan, W. Li, Z. Zhuang, Photocatalytic reduction of CO_2 to methane over HNb_3O_8 nanobelts, Appl. Catal. A- Gen. 413-414 (2012) 103–108.
[62] C.J. Wright, Inelastic neutron scattering spectra of the hydrogen tungsten bronze $H_{0.4}WO_3$, J. Solid State Chem. 20 (1977) 89–92.
[63] Y. Kuwahara, Y. Yoshimura, K. Haematsu, H. Yamashita, Mild deoxygenation of sulfoxides over plasmonic molybdenum oxide hybrid with dramatic activity enhancement under visible light, J. Am. Chem. Soc. 140 (2018) 9203–9210.
[64] Y. Su, Z. Han, L. Zhang, W. Wang, M. Duan, X. Li, Y. Zheng, Y. Wang, X. Lei, Surface hydrogen bonds assisted meso-porous WO_3 photocatalysts for high selective oxidation of henzylalcohol to benzylaldehyde, Appl. Catal. B- Environ. 217 (2017) 108–114.